Jet Propulsion Laboratory
California Institute of Technology

OPERA Algorithm Theoretical Basis Document for Coregistered Single Look Complex from Sentinel-1 data

Initial Release v1.1

June 26, 2024

JPL D-108752

Heresh Fattahi, Virginia Brancato, Seongsu Jeong

National Aeronautics and
Space Administration
Jet Propulsion Laboratory
California Institute of Technology
Pasadena, California

Signature Page

Prepared by:

Electronic Signature on File	9/3/2024
Heresh Fattahi, OPERA ADT Lead	Date
Electronic Signature on File	9/13/2024
Virginia Brancato, OPERA ADT Engineer	Date
Electronic Signature on File	9/4/2024
Seongsu Jeong, OPERA ADT Engineer	Date

Approved by:

Electronic Signature on File	8/29/2024
Steven Chan, OPERA Project Scientist	Date
Electronic Signature on File	8/29/2024
David Bekaert, OPERA Project Manager	Date

DOCUMENT CHANGE LOG

Revision	Cover date	Section changed	ECR #	Reason
Preliminary (v0.1)	September 12, 2022	All	N/A	New document, LRR067541.
v1.0	September 30, 2023	Sec. 2, 3, 6	N/A	Revised algorithm and timing corrections description, updated description of workflow input and output data, added Sec. 6 on performance assessment.
v1.1, Initial release	June 26, 2024	Sec. 2, 3	N/A	Added description of burst ID determination Added static layer algorithm. Minor editorial comments. URS clearance number: CL#24-1572

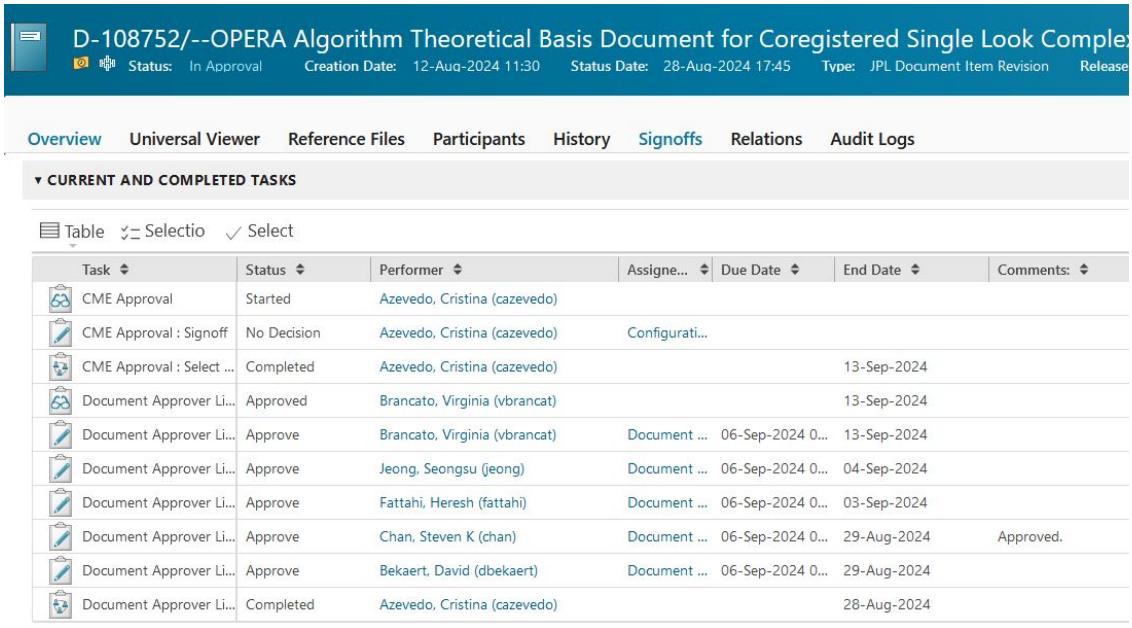

Aknowledgement

The research was carried out at the Jet Propulsion Laboratory, California Institute of Technology, under a contract with the National Aeronautics and Space Administration (80NM0018D0004).

1 Introduction

Synthetic Aperture Radar (SAR) is an active remote sensing technique used to monitor the Earth system and its spatial and temporal dynamics. SAR data acquired from a variety of spaceborne missions have been consistently used to estimate time-dependent vegetation biomass changes and disturbance [1], soil moisture [2], the extent of surface water [3], and to detect, classify, and track sea ice and polar ice dynamics [4, 5].

Repeat-pass Synthetic Aperture Radar Interferometry (InSAR) combines two SAR images acquired at different times and with similar acquisition geometries to form interferograms. SAR interferograms can be used to extract measurements of ground surface motion with a millimeter to centimeter accuracy [6]. The versatility of InSAR is evident through its successful application in different fields including the analysis of surface displacement resulting from earthquakes, tectonics, mining [7], volcanic activities [8], landslides [9], underground water reservoir discharge or recharge [10], and mountain glacier and ice sheets velocity tracking [11].

Raw data acquired from repeat-pass SAR missions are typically focused to generate a Single-Look Complex (SLC) image in its native range-Doppler grid [12]. This grid consists of a two-dimensional coordinate system, with image pixels arranged in the azimuth (along-track) and slant-range (across-track) directions [12]. Due to the slight separation between the orbits of temporally distinct SAR acquisitions, the range-Doppler grids of SAR images acquired over the same geographical area, typically exhibit misalignement [12]. The primary goal of SAR coregistration is to align the range-Doppler grids of two or multiple SLCs with sub-pixel precision ensuring that the corresponding pixels within the SLC stack correspond to identical targets within the scene [6]. To form coherent interferograms and prevent additional noise stemming from SLC misalignement, it is crucial to obtain a coregistration accuracy better than a fraction of the SLC pixel spacing [13].

Traditional coregistration algorithms are typically data-driven and rely on coherent or incoherent cross-correlation techniques. These techniques estimate the shift between a pair of SLCs by maximizing the cross-correlation of complex or SLC amplitude image patches. Coregistration algorithms rooted in data-driven approaches are known for being computationally expensive and the accuracy of the estimated shift is notably influenced by the quality of the cross correlation and interferometric phase i.e., the interferometric coherence [14]. Furthermore, data-driven cross-correlation algorithms may fail if the pair of SAR images is poorly correlated or when is affected by a large shift due to atmospheric propagation delays or inaccuracies in the sensor orbit state vectors.

An alternative to data-driven algorithms involves the coregistration of pairs of SLCs through a geometric mapping between ground and radar coordinates. Geometry-based coregistration algorithms estimate the slant range and azimuth positions of a ground target in both the reference and secondary SLC using the sensor orbit ephemeris and a Digital Elevation Model (DEM) [15]. Offsets derived from geometry-based coregistration may be affected by inaccuracies in the sensor's orbit and DEM, by microwave propagation delays in the Earth's atmosphere, by Earth surface motion (e.g., tectonic displacement), and by SAR image distortions caused by approximations made during SAR raw data focusing (e.g., the stop-and-go assumption) [15]. These misregistration errors can be mitigated by using data-driven coregistration algorithms [16] or by adding spectral diversity processing in both slant range and azimuth directions [17, 16].

Building upon the geometry coregistration framework, the Model-Adjusted Geometric Image Coregistration (MAGIC) algorithm corrects misregistration errors using model predictions [18]. Unlike data-driven techniques, MAGIC relies solely on the SAR data to be coregistered, eliminating the need for SAR images cross-correlation or spectral diversity. This not only provides a significant computational advantage but also frees the coregistration accuracy from being constrained by the amplitude cross correlation or interferometric phase quality. MAGIC's user-friendly interface, streamlined workflow, and faster runtimes make this algorithm an optimal choice for operational data systems. MAGIC's coregistration accuracy can be assessed by evaluating the relative geolocation error across a stack of SLC images. Recent studies on Sentinel-1 (S1) data have reported an accuracy of 6 cm and 26 cm in the slant range and azimuth directions, respectively [19, 18]. Such high relative geolocation accuracy allows coregistering S1 SLC data in radar coordinates with sub-pixel accuracy.

A more recent coregistration technique, the Geocoded Single-Look Complex (GSLC) has facilitated the generation and distribution of SLC data from the conventional range-Doppler grid to a more user-accessible map coordinates grid (i.e., geocoded grid) [20]. GSLC images can be produced using two distinct algorithms: 1) direct focusing of SAR raw data onto a geographical grid [21]; 2) resampling an existing range-Doppler SLC onto an user-defined geographical grid. The latter approach aligns with the Operational Product for End-user from Remote sensing Analysis (OPERA) project, aimed at converting Level-1 (L1) S1 SLC products into analysis-ready Level-2 (L2) Coregistered Single-Look Complex (CSLC) products. The OPERA L2_CSLC_S1 product is derived from S1 radar observations by geocoding each S1 burst on a geographical grid fixed in time. The L2_CSLC_S1 serves as an intermediate product for the generation of displacement maps over North-America and United States (US) territories.

This document provides an in-depth description of the algorithm employed

for generating OPERA's L2_CSLC_S1 products. Subsequent sections describe the algorithm's implementation, its underlying mathematical assumptions, their implications on data quality, and relative and absolute geolocation accuracy. Furthermore, the document delves into the algorithm's input data and the output products generated by the CSLC-S1 algorithm.

2 CSLC-S1 Algorithm

2.1 Background

The S1 mission employs the Terrain Observation with Progressive Scan (TOPS) technique to acquire SAR data in the Interferometric Wide (IW) and Extra Wide (EW) swath modes. The TOPS IW technique achieves wide swath widths ($\approx$ 250 km) typical of Scanning SAR (ScanSAR) while enhancing radiometric performance [22]. This wide swath width is achieved by acquiring bursts of echoes, i.e., by using sub-apertures, so that the antenna beam is cyclically switched in elevation to point at different range sub-swaths [22]. In contrast to ScanSAR, the TOPS mode electronically adjusts the beam's azimuth direction from backward to forward for each burst. This azimuthal steering equalizes the Signal-to-Noise ratio (SNR) and mitigates the scalloping effect often observed in ScanSAR acquisitions [22]. The European Space Agency (ESA) distributes IW and EW data as one image per sub-swath, for a total of three images [23]. Each sub-swath consists of a series of bursts, where each burst was processed as a separate SLC image. Adjacent bursts and sub-swaths share a common valid data region and are separated by an integer number of pixels.

The algorithm generating OPERA L2_CSLC_S1 products, hereafter indicated as CSLC-S1 algorithm, projects a S1 burst SLC from its native range-Doppler geometry onto an uniformly spaced north-south, and west-east aligned Universal Transverse Mercator (UTM) grid with a spacing in East and North directions comparable to the full resolution input SLC.

2.2 Algorithm description

The CSLC-S1 algorithm operates on the input S1 burst SLC images. In order to produce a burst of geocoded SLC data, the CSLC-S1 algorithm performs the following processing steps:

1 *Identify the burst identification (burst ID)*: Compute the unique identifier of the input burst SLC.

2 *Geocoded output grid bounding box*: lookup a predefined database of burst IDs based on the computed ID in the previous step to extract the predefined geocoded bounding box for the burst of interest.

3 *Inverse mapping*: Starting from the output grid defined in the previous step, calculate the slant range and azimuth time coordinates for every pixel in the geocoded output grid of the L2_CSLC_S1 product.

4 *Corrections*: Computes a set of low-resolution Look-Up Tables (LUTs) to correct the estimated slant range and azimuth times in Step #3 for known timing biases. These biases may stem from approximations made during S1 raw data focusing [19], from environmental effects[18], and from known displacement contributions (e.g., solid Earth tides) [24].

5 *Deramping*: Demodulates data in the azimuth direction.

6 *Sinc interpolation*: Interpolates data from Step #3 using a sinc interpolation kernel to find the data value at the slant range and azimuth time locations of interest.

7 *Reramping*: Evaluates the phase ramp of Step #3 at the range and azimuth locations of interest and adds it back to the interpolated data from Step #4.

8 *Flattening*: Removes the geometrical phase due to topography and flat Earth contributions from the data in Step #5.

9 *Geocode*: Assigns data in Step #6 to pixels in the geocoded grid.

The following subsections provide a detailed description of the CSLC-S1 algorithm processing steps.

2.2.1 Compute burst identification

The burst-id is determined as [25]:

$$burst-id = 1 + \left\lfloor \frac{\Delta t_b - T_{pre}}{T_{beam}} \right\rfloor \tag{1}$$

where t_{pre} is the preamble time interval and is fixed to $2.299849 sec$ for IW mode, t_{beam} is the interval of one burst and is fixed to $2.758273 sec$ for IW mode,

and Δt_b is the time distance between scene center (t_b) and the first Ascending Node Time (t_{ANX}) in the current mission cycle and computed as:

$$\Delta t_b = t_b - t_{ANX} + (r-1)\,T_{orb} \tag{2}$$

where r is the relative orbit number and T_{orb} is the nominal orbit duration assuming a cycle of 12 days for 175 orbits (i.e., $T_{orb} = 12 * 24 * 3600/175$ which equals 5924.5714285 sec). t_b is extracted from the time tag of the input S1 SLC data and the t_{ANX} can be either extracted from the S1 SLC metadata or can be computed from the orbit state vectors covering the scene of interest. The t_{ANX} included in the ESA's SAFE files metadata can be sometime off by 1-2 sec. Given the short duration of each burst around 2.7 sec, such biases in t_{ANX} leads to an offset in determination of burst-id. To mitigate the potential impact of incorrect t_{ANX} values on burst-id computations, we determine t_{ANX} by leveraging orbit state vectors. To achieve this, we conduct a search within the orbit coverage of the SLC data to identify the ascending node time, which denotes the time when the satellite crosses the equator from the ascending path. Given that a single orbit file may encompass multiple orbits, our search for t_{ANX} may yield multiple ascending node times. To narrow down the selection, we constrain the search to identify the ascending node time closest to the acquisition time and occurring prior to the acquisition moment.

2.2.2 Define output geocoded grid

To establish the geocoded grid for each burst, we construct a static database containing burst IDs alongside their corresponding geocoded grids. To construct this database, we extract the bounding polygon from ESA's burst map, calculate its centroid, and identify the UTM projection's EPSG code relevant to the burst in question. We assign EPSG 3413 (Sea Ice Polar North) for bursts covering Greenland and latitudes north of 75N and EPSG 3031 (Antarctic Polar Stereographic) for latitudes south of 60S. We determine the bounding coordinates for each burst by computing the minimum and maximum latitude and longitude of the burst polygon. Subsequently, we convert these coordinates to the projection system's coordinates using the respective EPSG code. To ensure that the output grid fully covers the burst data, we add 5 km margin to the computed bounding. We discretize the bounding coordinates to multiples of 30 meters. This discretization ensures that the resulting bounding box aligns with integer multiples of product spacing, such as 1, 2, 2.5, 3, 5, 6, 10, 15, or 30-meter increments, facilitating compatibility with various output products.

2.2.3 Inverse mapping

The initial step of the CSLC-S1 algorithm involves performing an inverse coordinate mapping i.e., from geocoded map coordinates to the range-Doppler coordinates. In this step, the algorithm calculates the slant range and azimuth time radar coordinates for each location of the geocoded output grid of a L2_CSLC_S1 product. Figure 1 provides a graphical overview of the SAR imaging geometry inherent to the inverse mapping problem. The red curve in Figure 1 represents the reference ellipsoid World Geodetic System 1984 (WGS84) while $S = (x_S, y_S, z_S)$ represents the radar sensor position in an Earth-centered Earth-fixed (ECEF) coordinate system, and $T = (x_T, y_T, h(x_T, y_T))$ is the target position referenced to the ellipsoid. $h(x_T, y_T)$ represents the topographic height at target location interpolated from a DEM at the horizontal coordinates of the target (x_T, y_T).

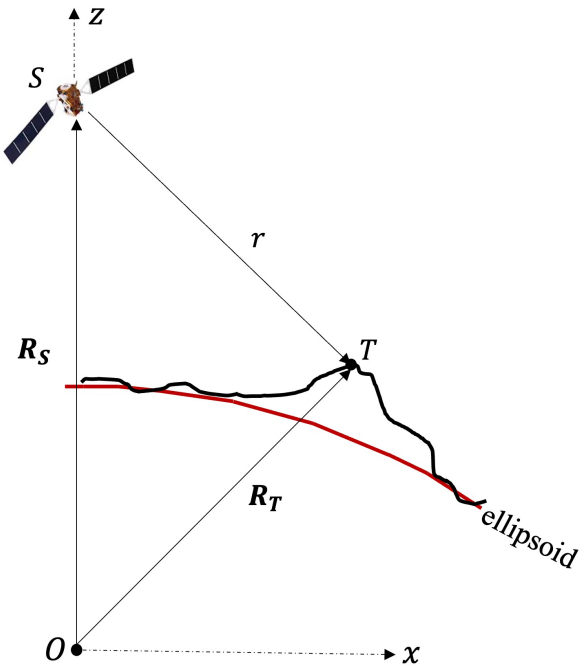

Figure 1: SAR imaging geometry in the Doppler centroid plane. $\mathbf{R_S}$ is the position vector of the SAR platform while $\mathbf{R_T}$ is the position vector of the target on the ground. r represents the slant range distance.

In a geocentric Cartesian coordinate system, the positions of the sensor and target are related by the range-Doppler equations:

$$\frac{2V_S(t)\cdot(\mathbf{R_T}-\mathbf{R_S}(\mathbf{t}))}{\lambda r} = f_{DC}(t,r) \tag{3}$$

$$r = |R_S - R_T| \tag{4}$$

where λ is the radar wavelength, $f_{DC}(t,r)$ represents the Doppler centroid of the target at the azimuth time (slow time) t and slant range (fast time) r , $V_S(t)$ is the sensor velocity, and $\mathbf{R_T}(t)$ and $\mathbf{R_S}(t)$ are the target and sensor position vectors at the azimuth time t, respectively. In Equation 4, $|\cdot|$ represents the L_1 norm. ESA provides S1 burst SLCs in a zero-Doppler image grid [23]. Therefore, for each slant range and azimuth time location, $f_{DC}(t,r) = 0$.

Knowing the S1 orbit ephemeris, the sensor velocity $V_s(t)$, and the target position T, the non-linear range-Doppler equations can be solved to estimate the slant range and azimuth time coordinates satisfying Equation (3). The S1 orbit ephemeris is generated by an on-board navigation solution and stored within the S1 L1 products. The orbit ephemeris is later refined by the Copernicus Precise Orbit Determination (POD) service. S1 orbit ephemeris files are available in the form of:

1. *Precise Orbit Ephemeris (POE)*: delivered within 20 days after the S1 data acquisition.

2. *Restituted Orbit Ephemeris (ROE)*: delivered within 3 hours after the S1 acquisition.

The ROE and POE orbit files provide the S1 sensor position and velocity with a 10 seconds temporal sampling and spanning a time interval of several hours with enough coverage before and after the S1 acquisition. Several analyses show that the difference in geolocation quality using ROE or POE is less than 3 cm [19], making the ROE orbit files sufficient for meeting the OPERA geolocation requirements. We use POE orbits if they are available which is the case when processing most archived data. For forward processing the new acquisitions we use ROE orbits to meet short latency requirements.

Given a known location on the ground, the inverse mapping algorithm starts from an initial azimuth time (e.g., burst center time) and interpolates the orbit state vector to extract the sensor position S and the platform velocity $V_S(t)$ at that azimuth time t. Since Equation (3) and Equation (4) are nonlinear, the inverse mapping algorithm performs an iterative search (e.g., Newton-Raphson) over the azimuth time t until convergence, i.e., when the difference between the

estimated azimuth time from the latest iteration and the previous iteration is smaller than a given threshold (e.g., $10e^{-8}$ seconds) [15]. Using the sensor position at t, the corresponding slant range r is computed from Equation (4). At convergence, the estimated azimuth time $\hat{t}$ and slant range $\hat{r}$ can be converted to a pixel location along the rows (n) and along the columns (m):

$$n = (\hat{t} - t_0) \cdot f_{PRF} \tag{5}$$

$$m = (\tau_{\hat{r}} - \tau_{r_0}) \cdot f_{RSF} \tag{6}$$

where f_{PRF} represents the Pulse Repetition Frequency (PRF) and f_{RSF} is the Range Sampling Frequency (RSF), t_0 represents the azimuth start time of the radar grid, τ_{r_0} is the fast time of the starting slant range (i.e., nearest range) of the radar grid, and $\tau_{\hat{r}}$ is the fast time of $\hat{r}$.

2.2.4 Timing corrections

The estimated slant range and azimuth times derived from the inverse mapping algorithm are susceptible to potential biases arising from various sources. These sources include inaccuracies in the DEM and sensor positioning, time delays caused by Earth's surface motion (e.g., solid Earth tides), and propagation delays due to the Earth's atmosphere (i.e., ionospheric and tropospheric delays). Furthermore, approximations made during S1 data focusing can introduce additional sources of geolocation inaccuracy [26]. ESA distributes L1 burst SLCs focused with a range-Doppler algorithm [23, 19]. During SAR image formation and product annotation processes, the ESA Instrument Processing Facility (IPF) processor employs some approximations in favor of processing runtime efficiency [27]. However, these approximations, combined with the limited update rate of certain spatially-variable processing parameters, can lead to offsets and distorsion in the distributed L1 SLC bursts [24]. For instance, the IPF processor does not fully account for the motion of the sensor platform during the signal propagation time (i.e., the stop-and-go approximation), the squint angle/Doppler effects, or the variation in topographic height during TOPS observations [26, 24]. These IPF approximations may reduce the geolocation accuracy of S1 products [19].

The following subsections delve into the characteristics of these various sources of geolocation inaccuracy and outline the algorithms used to correct them during the generation of L2_CLSC_S1 products.

2.2.4.1 Doppler-induced range shift correction

The fundamental principle underlying SAR is rooted in the dynamic change in distance between the sensor and the target under observation [12]. Consequently, the radar pulses transmitted and received by a SAR sensor experience a Doppler frequency shift, stemming from the motion of the sensor platform [12]. This frequency shift is ignored by the IPF processor during SAR image formation [27]. For S1 stripmap data, wherein the azimuth spectrum is almost centered at zero Doppler, this frequency shift cancels completely during range compression [19] as the frequency shift changes from positive to negative as the sensor approaches and then moves away from the imaged target over the course of synthetic aperture formation [19]. However, the TOPS mode captures SAR raw data featuring a substantial variation in the Doppler centroid in the along-track direction [22]. Particularly noteworthy is the pronounced Doppler centroid variation at the edge of S1 burst SLCs. This pronounced Doppler centroid variation is not factored into the IPF range compression, resulting in a proportional partial shift of the compressed range pulses [19]. Due to the cumulative effect of Doppler shifts across the entire swath, this range Doppler shift cannot be corrected during range compression (e.g., with the application of a range matched filter) but it is generally corrected during the post-processing of S1 data [24]. Failure to account for the correction of the Doppler-induced range shift can lead to shifts in the S1 data ranging between ± 0.4 m across each S1 burst [19].

The algorithm correcting the Doppler-induced range shift reconstructs the Doppler centroid $f_{DC,g}$ within the focused SLC burst at the grid coordinates (t_g, τ_g) taking into account the beam steering inherent to the TOPS acquisition mode. Subsequently, the Doppler centroid frequency $f_{DC,g}$ is scaled by the Frequency Modulation (FM) rate of the range chirp [19]. The Doppler-induced Range Shift (DRS) correction $\Delta\tau_{DRS}$ in range time can be expressed as:

$$\Delta\tau_{DRS} = \frac{f_{DC,g}}{K_r} \tag{7}$$

where K_r represents the range chirp rate. The Doppler-induced range shift correction needs to be added to the IPF annotated range times to compensate for the effect across the range times provided by the S1 annotation τ_{IPF}:

$$\tau_{corrected} = \tau_{IPF} + \Delta\tau_{DRS} \tag{8}$$

2.2.4.2 Bistatic azimuth delay correction

The ESA IPF processor adopts a stop-and-go approximation [12] when focusing the S1 raw data using a spectral-based image formation algorithm [27]. The stop-and-go approximation disregards the bistatic nature of S1 acquisitions assuming that the pulse duration is short enough to consider the sensor platform fixed during the transmission and reception of radar echoes [12]. However, during the transmission and reception of radar echoes the S1 platform moves approximately 30-40 m [19]. Therefore, all the range measurements within one single window are attributed to a single azimuth timing annotation [19]. This annotation is deduced from the Pulse Repetition Interval (PRI) that governs the echo window's duration [19]. To address the implications of the stop-and-go approximation, the IPF processor applies a bulk correction to adjust the azimuth timing annotation. However, this simple shift introduces a sub-pixel distortion and a range-dependent shift along the azimuth direction of approximately 2-4 m [19].

The algorithm correcting for the bistatic azimuth delay reconstructs the mid-swath (i.e., IW2) slant range time τ_{mid}. This parameter defines the IPF bulk correction, which is derived from the S1 product annotation as:

$$\tau_{mid} = \tau_{0,mid} + \frac{m_{mid} - 1}{2 f_{RSF,mid}} \tag{9}$$

where $\tau_{0,mid}$ represents the first range time of the mid-swath, m_{mid} is the number of range samples of the mid-swath, and $f_{RSF,mid}$ is the range sampling frequency at the mid-swath. The bistatic azimuth delay correction Δt_{BA} for a range time grid location τ_g at instant zero-Doppler is derived as:

$$\Delta t_{BA} = \frac{\tau_{mid}}{2} + \frac{\tau_g}{2} - rank \cdot t_{PRI} \tag{10}$$

where $rank$ represents the number of traveling pulses, and t_{PRI} is the pulse repetition interval. The zero-Doppler azimuth time of a burst sample at azimuth and range indices (n, m) is corrected as:

$$t(t_g, r_g) = t_{IPF}(n) + \Delta t_{BA} \tag{11}$$

where t_{IPF} represents the zero-Doppler azimuth time extracted from the S1 annotation.

2.2.4.3 Azimuth FM-rate mismatch correction

The azimuth geolocation accuracy can also be influenced by the inaccurate modeling of the azimuth Doppler FM-rate during the IPF raw data focusing pro-

cess [24]. In the case of spaceborne curved orbits, the distance between the sensor and the imaged target is affected not only by the closest approach range but also by the orientation of the Line-Of-Sight (LOS) with respect to the orbital plane. This introduce a dependency of the azimuth FM-rate on the topographic height of the observed target [24].

Spectral focusing algorithms, along with their transfer function formulation, rely on the assumption of a linear sensor flight path and the concept of effective velocity. This effective velocity parameter, which forms the basis for calculating the azimuth FM-rate, is held constant throughout the processing of large azimuth blocks during the IPF focusing processing step [19]. For SAR raw data with an azimuth spectrum centered at zero-Doppler (i.e., yaw-steered S1 stripmap mode), a discrepancy in the azimuth FM-rate results in defocusing (i.e., image blurring) and introduces a phase offset termed quadratic phase mismatch [12]. For S1 TOPS data, an azimuth FM-rate mismatch also introduces a shift in the along track-direction. A difference of 1000 m between the actual and assumed topographic height during IPF image formation can induce azimuth shifts up to 1 cm [19].

The algorithm correcting the azimuth FM-rate mismatch in TOPS data reconstructs the azimuth FM-rate k_a applied by the IPF processor. Specifically, this correction is computed during post-processing by analyzing the difference between k_a and the true azimuth FM-rate $k_{a,true}$, derived from the orbit-to-grid point geometry. Through a series of geometric considerations, the true azimuth FM-rate $k_{a,true}$ can be calculated as [24]:

$$k_{a,true} = \frac{2f_0}{c|R_s - R_g|}[(R_s - R_g) \cdot A_s + V_s \cdot V_s] \tag{12}$$

where f_0 is the S1 radar center frequency and R_s, V_s, and A_s represent the satellite position, velocity, and acceleration at the azimuth time of the correction grid t_g. The azimuth time correction to account for the azimuth FM-rate mismatch, Δt_{FMM} , can be expressed as [24]:

$$\Delta t_{FMM} = f_{DC,g} \cdot (-\frac{1}{k_{a,g}} + \frac{1}{k_{a,true}}) \tag{13}$$

where $f_{DC,g}$ represents the Doppler centroid frequency at the grid location t_g and $k_{a,g}$ is the annotated azimuth FM-rate at grid location t_g.

2.2.4.4 Solid Earth tides correction

SAR geodetic measurements of the Earth's surface are affected by the spatial and temporal dynamics of the solid Earth tides (SET) [28]. SETs are deforma-

tions of the Earth's crust caused by the gravitational force of the Sun and the Moon. These deformations comprise a vertical component with a typical magnitude of ≈ 20 cm, as well as a horizontal component, which can reach magnitudes up to 6 cm [29]. A comprehensive understanding of SET is expounded upon in Section 7.1.1 of the 2010 International Earth Rotation and Reference Systems Service (IERS) Conventions [29]. The CSLC-S1 algorithm uses the software package pySolid (`https://pypi.org/project/pysolid/`) to compute the 3-D tidal displacement vector in units of meters [18]. In particular, pySolid provides the SET displacement components in Easting (r^e_{SET}), Northing (r^n_{SET}), and up (r^u_{SET}) (ENU) with an accuracy of less than 1 mm [18]. These displacement components are converted into slant range and azimuth times over the timing correction grid. The algorithm performing this conversion solves the azimuth equation of zero-Doppler for the tide-corrected grid positions and it can be summarized by the following steps:

1. Use pySolid over a coarse (e.g., 5 km x 5 km) geographical grid covering the burst on the ground to get the SET displacement in ENU.

2. Convert the ENU SET displacement in a slant range and azimuth component. For every point of the geographical grid in Step #1 with latitude ρ, longitude ϕ, and height h:

   (a) Compute the ECEF coordinates of the point before applying the SET correction.

   (b) Calculate the ENU unit vectors in ECEF coordinates using the equations:

$$\mathbf{u}_{ecef} = \begin{bmatrix} cos(\phi)cos(\rho) \\ sin(\phi)cos(\rho) \\ sin(\rho) \end{bmatrix} \tag{14}$$

$$\mathbf{n}_{ecef} = \begin{bmatrix} -cos(\phi)sin(\rho) \\ -sin(\phi)sin(\rho) \\ cos(\rho) \end{bmatrix} \tag{15}$$

$$\mathbf{e}_{ecef} = \mathbf{n}_{ecef} \times \mathbf{u}_{ecef} \tag{16}$$

   (c) Scale the ENU unit vectors in Step #*b* with each component in the SET ENU vector to get the displacement by SET in ECEF.

   (d) Determine the ECEF coordinate of the point after the SET correction by adding to the vector in Step #*a* the vector calculated in Step #*c*.

   (e) Convert the ECEF coordinates of the point in Step #*d* into a latitude, longitude, and height coordinate system.

(f) Using inverse mapping algorithm described in section 2.2.3, estimate the azimuth time t and the slant range time τ of the point in Step #*a*.

(g) Using inverse mapping algorithm, estimate the azimuth time t_{SET} and the slant range time τ_{SET} of the point in Step #*d*.

(h) The difference of the slant range and azimuth time from Step #f and Step #g gives the displacement in the radar grid caused by SET.

2.2.4.5 Ionospheric delay correction

The ionosphere is a layer of the Earth's atmosphere located at altitudes approximately ranging from 100 km to 1000 km. The solar radiation at these altitudes may ionize the atmospheric atoms and molecules, thereby generating free electrons. The Total Electron Content (TEC) density varies with the altitude with a maximum free electron density around 300 km [30]. In addition to its dependency on altitude, the ionosphere's TEC varies with the geographical location, time of the day, season, and level of geomagnetic and solar activities [31]. The ionosphere is strong in the equatorial ionization anomaly crests and troughs, and at high latitude regions, and is generally weaker in the mid-latitude regions [31]. Table 1 summarizes the ionospheric spatiotemporal variation and its impact on S1 data [18].

Vertical TEC (Ionospheric range delay)	**Ascending Orbit (≈6 PM local solar time)**	**Descending Orbit (≈ 6 AM local solar time)**
2014 (solar maximum)	7 - 74 TECU (0.1 - 1.1 m)	7 - 21 TECU (0.1 - 0.3 m)
2019 (solar minimum)	3 - 22 TECU (0.0 - 0.4 m)	2 - 10 TECU (0 - 0.2 m)

Table 1: Expected ionospheric range delay in S1 C-band data based on GNSS-based ionospheric TEC variations during the last solar minima (2019) and maxima (2014). Values in this table are based on the statistical analysis of the JPL low-resolution Global Ionospheric Maps (GIM) [18].

In a first order approximation, the single-path absolute ionospheric delay in the LOS direction, r_{iono}, can be expressed as:

$$r_{iono} = TEC \cdot \frac{K}{f_0^2} \tag{17}$$

where $K = 40.31\ m^3 s^{-2}$ is a constant, f_0 is the radar transmitting frequency, and TEC represents the number of free electrons in a 1 m^2 cross section along the

slant range from the ground to the sensor platform. Adopting the widely used thin-shell assumption of the effective ionosphere layer, as shown in Figures. 5 and 6 in [18], the TEC at the ionospheric piercing point (IPP), i.e., the intersection of the radar LOS vector with the thin-shell ionosphere in (ρ_{IPP}, Φ_{IPP}), can be calculated from the vertical TEC (VTEC) products derived from the global navigation satellite system (GNSS) dual-frequency observations as:

$$TEC = \frac{VTEC(\rho_{IPP}, \Phi_{IPP})}{cos(\eta_{IPP})} \tag{18}$$

where ρ and Φ are the latitude and longitude, respectively; η_{IPP} is the refraction angle of the LOS vector at IPP. η_{IPP} can be calculated from the incidence angle at IPP, θ_{IPP}, following Snellś law as:

$$\eta_{IPP} = arcsin(\frac{n_0}{n_{iono}} sin(\theta_{IPP})) \tag{19}$$

where $n_0 = 1$ is the refractive index of vacuum and n_{iono} is the group refractive index of ionosphere. n_{iono} can be calculated to the first order from $VTEC$ [32] as:

$$n_{iono} = 1 + VTEC(\rho_{IPP}, \Phi_{IPP}) \cdot \frac{K}{f_0^2} \tag{20}$$

Assuming a spherical coordinate system, θ_{IPP} can be calculated from θ (the incidence angle of the LOS vector on the ground) as:

$$\theta_{IPP} = \arcsin(\frac{Re \cdot \sin(\theta)}{Re + h_{IPP}}) \tag{21}$$

where Re is the Earth radius, h_{IPP} is the effective height of the ionosphere, which is commonly set to 450 km [33]. Given the position of the target on the ground (ρ_T, Φ_T), the incidence angle θ and azimuth angle β of the LOS vector on the ground, the IPP position (ρ_{IPP}, Φ_{IPP}) can be calculated following standard geodetic formula [18].

2.2.4.6 Tropospheric delay

The troposphere is a layer of the Earth's atmosphere roughly situated at 30 km from the Earth's surface [34]. Microwave signals propagating through the Earth's troposphere experience a spurious signal path delay inducing absolute geolocation errors on the order of 1-4 m [18, 35].
The tropospheric delay is conventionally divided into two principal components, namely the hydrostatic and wet components [36]. The hydrostatic component primarily depends on the variation of the atmosphere refractive index due to

changes in air pressure [36]. These changes are in turn related to variations in the observed scene altitude [37]. In contrast, the wet troposphere componenent is attributed to the presence of atmospheric constituents like clouds and water droplets and exhibits a dependency on the water vapor pressure [36]. While the wet tropospheric delay exhibits a substantial spatiotemporal variability [34], the hydrostatic delay remains relatively stable, owing to the limited pressure fluctuations within the typical extent of a SAR image [36].

Many tropospheric delay correction algorithms are based on the use of global atmospheric models, such as those from the European Center for Medium-Range Weather Forecasts (ECMWF) [38]. However, the latency associated to the availability of these global weather models (e.g., 1-5 days) can pose restrictions to the real-time processing of operational data production systems.
The CSLC-S1 algorithm corrects for the effect of the tropospheric delay on geolocation using a simplified static troposphere model [39]. The model assumes that the tropospheric path delay depends only on the altitude and the incidence angle of the radar wave, according to the following equation:

$$r_{tropo} = \frac{ZPD}{\cos\theta} e^{-\frac{h}{H}} \tag{22}$$

where r_{tropo} is the slant range delay caused by troposphere, ZPD = 2.3 m represents a constant zenith path delay, θ represents the incidence angle, h is the scene topographic height, and H = 6000 m represents a reference height [40].

2.2.5 Azimuth deramping and demodulation

The distinguishing characteristic of the S1 TOPS mode is its ability to electronically steer the antenna in the along-track direction, ensuring that the targets are consistenly illuminated with the same azimuth antenna pattern [22]. This feature introduces a linear frequency modulation in both S1 raw and SLC burst data. The removal of this linear frequency modulation, known as deramping, is a crucial step to perform basic signal processing operations such as oversampling or interpolation.

The deramping procedure involves the multiplication of the burst SLC data with a chirp signal in the azimuth time domain [41]:

$$\phi(t,\tau) = e^{-j\pi k_t(\tau)(t-t_{ref}(\tau))^2} \tag{23}$$

The variable t denotes the zero-Doppler azimuth time, t_{ref} represents the reference azimuth time, and $k_t(\tau)$ characterizes the Doppler centroid rate within the focused TOPS burst data. The Doppler centroid rate is expressed as:

$$k_t(\tau) = \frac{k_a(\tau) \cdot k_s}{k_a(\tau) - k_s} \tag{24}$$

with k_a indicating the azimuth FM rate, which is always negative, while k_s denotes the Doppler centroid rate introduced by the electronic steering of the S1 antenna. The azimuth FM rate is provided as part of the S1 annotation metadata, and it is expressed as a sequence of range polynomial coefficients that are updated with the azimuth time t. The Doppler rate introduced by the antenna steering can be approximated as:

$$k_s \approx \frac{2V_{s,mid}}{\lambda} \cdot k_\psi \tag{25}$$

where k_ψ represents the azimuth steering rate of the antenna, measured in radians per second, and $V_{s,mid}$ represents the spacecraft velocity computed at the midpoint of the azimuth time by interpolating the orbit state vectors. Since k_s is not contingent upon range, it can be computed only once for each burst.
After the deramping step, the azimuth spectral content of the S1 data remains centered around the Doppler centroid frequency. To further process the data, it is necessary to perform a demodulation step i.e., the azimuth spectral content of the burst data is shifted to the low-pass portion of the spectrum, centered around 0 Hertz [41]. Deramping and demodulation can be effectively performed in tandem by updating Equation 23 [41]:

$$\phi(t,\tau) = e^{-j\pi k_t(\tau)(t-t_{ref}(\tau))^2 - j2\pi f_{DC}(\tau)\cdot(t-t_{ref}(\tau))} \tag{26}$$

The modified Equation 26 ensures that the azimuth spectral content of the S1 burst data is appropriately centered around 0 Hertz before performing subsequent processing steps [41].

2.2.6 Data interpolation

The data interpolation process consists of generating a continuous function from a discrete set of values within a 2-D array. The performance of an interpolation method is evaluated by its capacity to maintain the integrity of the original signal while performing the interpolation. Depending on the nature of the data being interpolated, subpar interpolation quality can lead to undesired effects such as data smoothing, ringing artifacts, alterations in image intensity, or increased interferometric phase noise.

The selection of an interpolation technique is often the result of a trade-off between interpolation quality and the resultant outcomes. The most common interpolation algorithms for complex-valued SLC data are:

1. *FFT-based oversampling followed by fast interpolation*: this method involves oversampling the data using a Fast Fourier Transform followed by rapid interpolation techniques like cubic spline interpolation.

2. *Direct interpolation using high-quality time domain methods*: Alternatively, direct interpolation can be performed using high-quality time-domain interpolation methods such as sinc or Lanczos interpolation.

To preserve the quality of the interpolated complex-valued signal, the CSLC-S1 algorithm adopts a sinc interpolation kernel.

2.2.7 Reramping

After the sinc interpolation process, it becomes necessary to evaluate Equation 26 at the interpolation coordinates and subsequently integrate the result with the interpolated complex-valued burst data. This integral part of the data processing is known as reramping. The rational behind reramping stems from the observation that the initial deramping and demodulation steps introduce a bias in the interferometric phase [41]. This bias emerges as a result of recentering the azimuth spectral content of the burst SLC data around 0 Hertz during deramping and demodulation. Consequently, to avoid this bias, the burst data must be brought back to their original spectral content through the reramping procedure [41].

2.2.8 Flattening

The phase component of the interpolated SLC data encompasses the phase information corresponding to the slant range distance existing between the radar sensor and the target. This phase component encapsulates contributions from both the topography and flat Earth phase [36]. To facilitate the use of L2_CSLC_S1 products in displacement time series processing, the CSLC-S1 algorithm undertakes the removal of these phase contributions (i.e., flattening) using the equation:

$$SLC_{flattened} = SLC_{unflattened} \cdot e^{j\frac{4\pi}{\lambda}r} \tag{27}$$

where $SLC_{unflattened}$ represent the SLC data prior to flattening, λ is the radar wavelength, while r represents the slant range distance between the map coordinates and the sensor.
It is important to note that the slant range in Equation 27 is not adjusted for the various delay components discussed in Section 2.2.4. Consequently, interferograms generated from OPERA L2_CSLC_S1 products will inherently contain

various environmental and geophysical delay components. These may include, but are not limited to, ionospheric and tropospheric delays, as well as contributions from solid Earth tides.

2.2.9 Static layer

The orbits of Sentinel-1 mission are well maintained so that the similar trajectory are repeated within the accuracy sufficient for interferogram formation. Therefore it is expected that the parameters derived from satellite's geometry and/or DEM does not significantly change over time for each burst product. With this rationale, CSLC-S1 provides line-of-sight (LOS) vector, layover/shadow mask, and local incidence angle as static layers.
The computation of the static layers starts from forward mapping, which is to map the range-Doppler coordinates to geocoded map coordinates. This procedure results in latitude, longitude, and height for every pixels in the radar coordinates. The timing of each lines in the radar coordinate is used to estimate the satellite's position by interpolating the orbit with respect to time. Given the position of the sensor and the estimated position of the target, the LOS vector from the ground target to the sensor is formed. The angular difference between this vector with the surface normal vector gives local incidence angle, where the surface normal is calculated from the DEM.

In order to identify pixels in shadow, we compute elevation angle, which is the angle between the LOS vector at sensor position with the nadir vector, for every range bin across the swath. We then walk over the slant ranges computing the gradient of the elevation angle with slant range increase and label pixels with negative elevation angle gradient as shadow. In order to identify pixels with layover we compute the ground range across the swath, sort them as a function of slant range for one line of data and evaluate gradient of the ground range computed at each pixel as the difference between the ground range at that pixel and the previous pixel. We label pixels with negative gradient as layover [42].

After the computation, they are geocoded with the algorithm described in 2.2.3 with either biquintic interpolation (for LOS, and local incidence angle) or nearest neighbor interpolation (for layover/shadow area).

2.3 Algorithm inputs

The inputs to the CSLC-S1 algorithm are listed in Table 2 and they encompass the following components:

- *S1 SAFE file*: The Standard Archive Format for Europe (SAFE) file for S1 products acquired in the IW mode contains individually focused burst SLC

images acquired by the ESA S1 sensors. The IW mode typically covers a 250 km swath with a single-look spatial resolution of 2.4 m in slant range direction and 20 m in azimuth direction. The IW mode captures 3 subswaths. ESA resamples all the bursts in the 3 subswaths to a common pixel space grid in both slant range and azimuth directions. This eliminates the need for further data interpolation in subsequent processing steps.
The input SAFE file also contains the S1 product metadata, typically distributed in annotation XML files. These include annotation files for all the 3 subswaths, calibration annotation files, noise annotation files, and Radio Frequency Interference (RFI) annotation files. These files provide essential processing information, radiometric calibration data, denoising data, and RFI detection and mitigation parameters and information.

- *S1 orbit ephemeris file*: S1 orbit ephemeris files contain information on the satellite position and velocity during radar sensor acquisition. This data is recorded by a Global Navigation Satellite System (GNSS). S1 orbit information generated by an onboard navigation solution are stored within the S1 L1 products. This orbit information is subsequently refined by the Copernicus POD service. S1 orbit ephemeris files are available as ROE and POE (see Section 2.2.3). The S1 orbit ephemeris files can be obtained from ESA Copernicus Dataspace (`https://dataspace.copernicus.eu/explore-data/data-collections/sentinel-data/sentinel-1`) or at the Alaska Satellite Facility (ASF) (`https://s1qc.asf.alaska.edu/`).

- *DEM*: The CSLC-S1 algorithm employs a static DEM for processing, which is based on the Copernicus DEM with a 30 m resolution (GLO-30 DEM), whose vertical datum was converted from EGM2008 (i.e. geoid) to WGS84 (i.e. Ellipsoidal height). This DEM corresponds to the DEM used for the NASA-ISRO SAR (NISAR) mission, often referred to as NISAR-DEM. This DEM can be overridden by an external user-provided DEM. The Copernicus GLO-30 DEM can be downloaded at Open Topography (`https://portal.opentopography.org/raster?opentopoID=OTSDEM.032021.4326.3`).

- *Ionosphere TEC maps*: The ionosphere TEC maps are products provided by the International GNSS Service (IGS). These maps provide daily insights into the spatial distribution of the VTEC across the Earth's ionosphere. The IGS TEC maps are derived from dual-frequency GNSS data, such as GPS and Galileo, and are typically distributed in the Ionosphere Exchange (IONEX) format. The IGS maps come in two categories:

  - *Rapid solution*: these TEC maps have low latency, with updates available in less than 24 hours. They provide timely information for near-real-time ionospheric monitoring and correction applications.
  - *Final solution*: Final Solution TEC maps have a latency of approximately 24 days. They are more accurate and refined compared to the rapid solutions TEC maps.

  To reduce latency without compromising the absolute geolocation performance, the CSLC-S1 algorithm uses Rapid Solution IGS (IGR) TEC maps. These maps can be obtained through the Crustal Dynamic Data Information System (CDDIS) (`https://cddis.nasa.gov/archive/gnss/products/ionex/`).

- *S1 burst database*: The S1 burst database is a crucial resource for the operational production of CSLC-S1 products. This database, maintained by the OPERA project, is structured as a SQLite file containing essential information about the bursts acquired worldwide during the course of the S1 mission.
  Given the systematic nature of burst acquisitions by the S1-A/B sensors, the geographical location of bursts on the Earth's surface remains almost identical during each satellite pass. Each burst is uniquely identified by an alphanumeric string referred to as the *burst identification number* or *burst ID*. These burst IDs adhere to the same convention employed by ESA when generating their burst map. In addition to burst IDs, the burst database also encompasses other pertinent processing information, including details about the relative orbit number, corner coordinates specifying the geographical extent of the burst, and the projection system employed for the geographical grid onto which each L1_CSLC_S1 product is generated.

  The utilization of the burst database during the production of L1_CSLC_S1 products ensures that a time-series of L1_CSLC_S1 products sharing the same burst ID are aligned on the same geographical grid.

  The burst database adopted in the production of L1_CSLC_S1 products is generated and maintained by the OPERA project and can be accessed from their GitHub repository (`https://github.com/opera-adt/burst_db`). The ESA burst map can be obtained from the following source: `https://sar-mpc.eu/files/S1_burstid_20220530.zip`.

Input data	Producer
S1 SAFE file	ESA
S1 orbit ephemeris	ESA
DEM Copernicus GLO-30	ESA and JPL
Burst data base	ESA and JPL
TEC maps	IGS and JPL

Table 2: Data inputs to the CSLC-S1 algorithm.

2.4 Algorithm outputs

The CSLC-S1 algorithm generates three distinct output products:

- *L2_CSLC_S1 product*: this product is directly derived from the L1 S1 burst SLC data. It is distributed as a HDF5 file conforming to the Climate Forecast (CF)-1.8. The L2_CSLC_S1 product comprises the following data layers:
  - *Geocoded complex backscatter*: a data layer consisting of complex-valued numbers representing the complex backscatter from the input S1 burst on a North-South, East-West aligned UTM/WGS84 geographical grid.
  - *Azimuth carrier phase*: a data layer containing the phase information corresponding to the linear frequency ramp caused by the electronic steering of the S1 sensor antenna in the along-track direction (see Section 2.2.5). This phase information is also provided on the same geographical grid as the complex backscatter. The removal of this linear frequency modulation is a crucial preprocessing step before performing basic operations such as interpolation and resampling.
  - *Flattening phase*: this data layer contains the phase information necessary for the complex backscatter flattening, taking into account a zero-height ellipsoid (i.e., ellipsoidal flattening) and the topographic height using a DEM (i.e., topographic flattening).

  Metadata in a L2_CSLC_S1 product is categorized into five sections:
  - *Product identification*: includes information for product identification, such as the product version and the product specification version.

  - *Input datasets*: provides details about the input datasets used in generating the product, including the name of the input S1 SAFE granule and the name of the orbit files used for processing.
  - *S1 input burst metadata*: contains relevant information about the input burst used in the product generation, including essential parameters for reconstructing the radar grid of the burst (e.g., starting range, pulse repetition frequency).
  - *S1 orbit ephemeris metadata*: containing information regarding sensor time, position, and velocity at the time of the burst acquisition.
  - *Processing metadata*: this section provides metadata related to the processing steps applied to generate the product, including a set of low-resolution Look-up Tables (LUT) containing the timing corrections used to improve the absolute geolocation of the product and information about the geographical grid of the product (e.g., projection system, spacing in the X-/Y-directions).

- *L2_CSLC_S1 Browse image*: this product is a grayscale geocoded Portable Network Graphic (PNG) image representing the amplitude of the L2_CSLC_S1 complex backscatter. It is generated on a latitude and longitude coordinates grid and typically features a transparent background.

- *L2_CSLC_STATIC*: this HDF5 files adheres to the CF-1.8 convention and includes full-resolution static data layers describing the acquisition geometry of the corresponding L2_CSLC_S1 product. The layers contained in L2_CSLC_STATIC include:

  - *East LOS unit vector*: a floating-point data layer containing the East component of the LOS unit vector from the target to the sensor.
  - *North LOS unit vector*: a floating-point data layer containing the North component of the LOS unit vector from the target to the sensor.
  - *Local incidence angle*: a floating-point data layer specifying the angle between the LOS vector and the normal to the target's local surface.
  - *Layover/shadow mask*: an unsigned integer layer used for flagging regions affected by the layover and shadow effects. In this layer, 0 denotes pixels unaffected by layover or shadow, 1 indicates pixels affected by shadow, 2 represents pixels affected by layover, and 3 indicates pixels affected by both layover and shadow.

  Metadata in a L2_CSLC_STATIC product are organized into 4 main HDF5 groups:

- *Product identification*: containing information for product identification. The structure of this group is consistent with that of a L2_CSLC_S1 product.
- *S1 orbit ephemeris data*: containing the sensor time, position, and velocity of the burst used for the generation of the product
- *Processing metadata*: containing relevant metadata describing the processing parameters characterizing the input burst and datasets summarizing the algorithm and processing steps used to generate the product.
- *Quality assurance information*: this group contains several statistical parameters (e.g., minimum, maximum, mean values) organized into individual HDF5 datasets for each two-dimensional dataset within the product.

The L2_CSLC_STATIC product is generated only once or a limited number of times to account for changes in the DEM, S1-A/B orbit ephemeris, or in the algorithm producing the product. S1 burst SLCs covering the same area on the ground (i.e., characterized by the same burst ID) share the same L2_CSLC_STATIC product.

3 Algorithm assumptions

3.1 Static DEM

The use of a static DEM in the production of L2_CSLC_S1 products offers advantages in terms of operational simplicity and computational efficiency. However, it comes with certain limitation and considerations:

- *Inaccuracy in terrain-varying areas*: the assumption of a static DEM implies that the topography of the Earth's surface remains constant throughout the production of L2_CSLC_S1 products. In reality, certain regions experience terrain variations due to natural events such as volcanic eruptions, landslides, or anthropogenic activities. In such cases, the use of a static DEM may lead to inaccuracies in topographic corrections, affecting the quality of interferograms generated with L2_CSLC_S1 products.
- *Reprocessing challanges*: any change in the DEM during the production of L2_CSLC_S1 products could necessitate reprocessing the entire L2_CSLC_S1 archive.

- *DEM data gaps and inaccuracies*: DEMs may contain gaps or inaccuracies especially over regions covering challenging terrains or over areas with limited data availability. While such errors typically have a negligible impact on SAR interferograms, they can become more pronounced in areas with challenging terrain features.

- *Coregistration accuracy*: in regions with challenging terrains or large terrain variations, DEM errors can introduce absolute coregistration inaccuracies. These inaccuracies can affect the alignment of SAR images and lead to challenges in accurately measuring ground displacement.

3.2 Sentinel-1 Level-1 Products Calibration from ESA

The L1 S1 SLC products provided by ESA undergo both internal and external calibration processes to ensure the accuracy and the consistency of the data.
The primary objective of internal calibration is to correct for the variations in amplitude and phase of the signal within the instrument. These variations can occur due to factors such as instrument geometry and internal stability. Hardware components are inherently not stable, and as a result, the internal variations in the signal phase need to be accounted for during the internal calibration processes. ESA conducts comprehensive internal calibration activities to minimize the instrument drifts within each burst. These activities are effective at achieving residual instrument drifts of less than 0.1 dB in amplitude and just few degrees in phase [43]. The precise internal calibration serves as the foundation for ensuring the overall stability of the instrument and is instrumental in achieving the required absolute radiometric calibration accuracy of 1 dB (with a 3σ confidence level) [43].

External calibration aims to establish a link between pixel intensity values within the S1 burst SLC data and physical quantities, such as the radar cross-section. ESA accomplishes this by computing calibration constants based on radiometric measurements obtained from transponders and reference targets. These measurements provide essential reference points for calibration. In addition to transponders and reference targets, measurements from homogeneous areas, such as rainforests, are also used to supplement the calibration process. External calibration ensures that the information contained in the S1 SLC burst data can be accurately converted into physical quantities, enabling meaningful scientific analysis and interpretation.

The accuracy of historical S1 granules can be influenced by residual calibration biases [44], which, in turn, can impact the absolute geolocation accuracy in the Easting and Northing directions of the generated L2_CSLC_S1 products. ESA

has undertaken several efforts to mitigate these biases, especially in the slant range direction. Starting from May 5, 2015, a correction for the slant range calibration bias was introduced into the IPF software [44]. However, L2_CSLC_S1 products generated from S1 granules prior to May 5, 2015, may be affected by absolute geolocation errors in the Easting and Northing directions ranging from 1 to 3 meters, depending on the specific S1 granule and time of acquisition [44]. Users and researchers working with L2_CSLC_S1 products generated from historical S1 data should be aware of this potential geolocation error and account for it when conducting geospatial analysis or utilizing the L2_CSLC_S1 products for applications that require high positional accuracy. For applications sensitive to geolocation accuracy (e.g., InSAR time series analysis), it may be advisable to use data acquired after the calibration bias correction [44].

3.3 Ionosphere-dominated azimuth misregistration errors

The CSLC-S1 algorithm does not correct for azimuth misregistration errors induced by ionospheric propagation. Although the azimuth shift caused by the ionosphere is smaller at C-band compared to L-band [45], these relatively small azimuth misregistration errors can still have notable consequences, particularly when stitching interferograms from adjacent bursts [46]. The ionosphere-induced azimuth misregistration errors can result in intra-burst phase jumps when combining interferograms from neighboring bursts. Due to the use of the TOPS imaging mode, the position of the imaged ionosphere differs from the position of the imaged target on the Earth's surface [22, 46]. This deviation varies azimuthally across the burst. Consequently, in mosaicked interferograms produced using L2_CSLC_S1 products, phase jumps may be observed at the burst edges. The estimation and compensation of these phase jumps can be performed during the ionosphere phase correction. Techniques such as the range split-spectrum can be employed for this purpose [47, 46]. It is worth noting that, in most cases, the azimuth shift induced by ionospheric effects does not lead to significant decorrelation in SAR interferograms [46]. However, addressing these phase jumps is essential for achieving accurate and reliable results in interferometric applications and geospatial analyses that rely on L2_CSLC_S1 products.

4 Algorithm implementation

The OPERA CSLC-S1 workflow is implemented in Python and is open-source. The code can be accessed through the Coregistered Multi-temPorAl Sar Slc (COMPASS) GitHub repository at `https://github.com/opera-adt/COMPASS`. COMPASS relies on three main software dependencies:

- *InSAR Scientific Computing Environment Enhanced Edition (ISCE3)*: The core functionality for geocoding the Sentinel-1 SLC images is coming from ISCE3 geocodeSlc module which was originally developed by the NISAR project. ISCE3 is an open-source software package implemented in C++ with Python bindings. It provides core modules and functionalities for interferometric and polarimetric processing, image geocoding, and SAR image focusing [48]. ISCE3 is the software used for the operational production of NISAR L1 and L2 data products [48]. ISCE3 is open-source and can be accessed through its GitHub repository `https://github.com/isce-framework/isce3` and as a Conda package at `https://anaconda.org/conda-forge/isce3`.

- *OPERA S1-reader*: The OPERA S1-reader is another open-source software component developed by the OPERA ADT team. The S1-reader is responsible for creating an ISCE3-compatible burst class object given a S1 SAFE file, polarization, and file path to the orbit directory. The S1-reader is responsible for parsing the S1 burst object with the metadata associated with the input S1 data. The created S1 burst object can be directly used to build processing workflows using the core modules available in the ISCE3 software. The S1-reader is accessible through its GitHub repository at `https://github.com/isce-framework/s1-reader`.

- *Python based solid Earth tides (PySolid)*: this software is a Python wrapper for Fortran *solid.for* program created by Dennis Milbert [49] which calculates the solid Earth tides in Easting, Northing, and Up directions. This software package does not introduce any new functionality to the underlying original Fortran code but it makes it easier to use from Python. PySolid is an open-source software accessible through its GitHub repository at: `https://github.com/insarlab/PySolid`.

5 Algorithm usage constraints

The CSLC-S1 Algorithm does not account for:

- Geolocation errors caused by significant ionosphere phase gradients along the azimuth direction.

- Errors in existing DEMs. Errors in the DEM can lead to geolocation inaccuracies, particularly in areas with challenging terrain features.

- DEM errors caused by major changes to the Earth's surface, e.g., collapse of the caldera of a volcano.

- Errors and artifacts caused by RFI

6 Performance assessment

The verification and validation process for the CSLC-S1 algorithm involves computing the absolute geolocation errors on a time-series of L2_CSLC_S1 products over regions including reference calibration targets e.g., corner reflectors. The location of these corner reflector targets is accurately monitored in time. The procedure for estimating the absolute geolocation error involves the following steps:

- *Correction for plate tectonics and solid Earth tides*: the coordinates of the surveyed corner reflector positions in the Easting and Northing directions, referred to as the predicted corner reflector positions, are corrected to account for plate tectonic drifts and solid Earth tides, if necessary. Those effects may cause a gradual shift in the position of the surveyed corner reflectors in time.

- *Extraction of complex backscatter area*: an area of 32x32 pixels is extracted from each L2_CSLC_S1 complex backscatter data. This extraction is centered around the coordinates of the predicted corner reflector position.

- *Measurement of corner reflector peak*: the Easting and Northing coordinates of the corner reflector peak within the 32x32 complex backscatter patch, referred to as measured corner reflector position, are determined by using a 128-times FFT oversampling of the complex backscatter data

- *Calculation of the absolute geolocation error*: the absolute geolocation error in both Easting and Northing direction is computed by taking the difference between the predicted and measured corner reflector positions along the corresponding axis. This error quantifies how accurately the CSLC-S1 algorithm geolocates the burst S1 data.

7 Data access

Data access input data:

- S1 IW SLC SAFE files provided by ESA and available for download through the Copernicus Open Hub `https://scihub.copernicus.eu/` or through the ASF Distributed Archive Center (DAAC) `https://asf.alaska.edu/`.

- S1 orbit files are provided by ESA and available through SciHub `https://scihub.copernicus.eu/gnss/#/home` or through the ASF DAAC `https://s1qc.asf.alaska.edu/`.
- Copernicus DEM GLO-30 available at `https://spacedata.copernicus.eu/`

Data Access Output Data:

- CSLC-S1 products and CSLC-S1 static layers products will be made available through the ASF DAAC.

8 Contacts

Heresh Fattahi
Jet Propulsion Laboratory, California Institute of Technology
Pasadena, CA, USA
heresh.fattahi@jpl.nasa.gov

Virginia Brancato
Jet Propulsion Laboratory, California Institute of Technology
Pasadena, CA, USA
virginia.brancato@jpl.nasa.gov

Seongsu Jeong
Jet Propulsion Laboratory, California Institute of Technology
Pasadena, CA, USA
seongsu.jeong@jpl.nasa.gov

9 Acronyms

ADT	Algorithm Development Team
ASF	Alaska Satellite Facility
BA	Bistatic Azimuth delay (timing correction)
CDDIS	Crustal Data Information System
CF	Climinate Forecast
COMPASS	COregistered Multi-temPorAl Sar Slc
CSLC	Coregistered Single Look Complex
DAAC	Distributed Active Archive Center
DC	Doppler Centroid
DEM	Digital Elevation Model
DRS	Doppler-induced Range Shift
ECEF	Earth-centered Earth-fixed
ECMWF	European Centre for Medium-Range Weather Forecasts
ENU	Easting, Northing, Up
ERA5	ECMWF Re-Analysis version 5
ESA	European Space Agency
EW	Extra Wide (S1 AB mode)
FM	Frequency Modulation
FMM	FM-rate mismatch (timing correction)
GIM	Global Ionospheric Maps
GLO-30	Global Copernicus DEM 30 m
GNSS	Global Navigation Satellite System
GSLC	Geocoded Single-Look Complex
HDF5	Hierarchical Data Format version 5
IERS	International Earth Rotation and Reference System
IGR	International GNSS Rapid Solution
IGS	International GNSS Service
InSAR	Interferometric SAR
IONEX	Ionosphere Exchange (data format)
IPF	Instrument Processing Facility
IPP	Ionosphere Piercing Point
ISCE3	InSAR Scientific Computing Environment Enhanced Edition
IW	Interferometric Wide (S1 mode)
JPL	Jet Propulsion Laboratory
L1	Level-1 product
L2	Level-2 product
LOS	Line of Sight

LRS	Limited Request System
LRR	Limited Request Release
LUT	Look-Up Table
MAGIC	Model-Adjusted Geometrical Image Coregistration
NASA	National Aeronautics and Space Administration
NISAR	NASA-ISRO SAR
POD	Precise Orbit Determination (Copernicus service)
POE	Precise Orbit Ephemeris
PNG	Portable Network Graphic
PRF	Pulse Repetition Frequency
PRI	Pulse Repetition Interval
PySolid	Python based solid Earth tides (software package)
OPERA	Operational Product for End-users from Remote sensing Analysis
RFI	Radio Frequency Interference
ROE	Restituted Orbit Ephemeris
RSF	Range Sampling Frequency
S1	Sentinel-1
S1AB	Sentinel1 AB
SAFE	Standard Archive Format for Europe
SAR	Synthetic Aperture Radar
ScanSAR	Scanning Synthetic Aperture Radar
SET	Solid Earth Tides
SLC	Single-Look Complex
SNR	Signal-to-Noise ratio
SQLite	Structure Query Language
TEC	Total Electron Content
TECU	TEC Unit
TOPS	Terrain Observation with Progressive Scan
US	United States
UTM	Universal Transverse Mercator
VTEC	Vertical TEC
WGS84	World Geodetic System 1984
XML	eXtensible Markup Language
ZPD	Zenith Path Delay

10 List of symbols

$\|\cdot\|$	L_1 norm
$rank$	Number of traveling pulses
A_S	Sensor acceleration
c	Speed of light
e	Water vapor partial pressure
f_0	Radar transmitting frequency
f_{DC}	Doppler centroid
$f_{DC,g}$	Doppler centroid at grid location point (t_g, τ_g)
f_{PRF}	Pulse repetition frequency
f_{RSF}	Range sampling frequency
$f_{RSF,mid}$	Range sampling frequency at mid-swath IW2
g_m	Weighted average of gravity acceleration between h and h_{ref}
$h(x_T, y_T)$	Topographic height at horizontal coordinates (x_T, y_T)
h	Elevation of interest
h_{IPP}	Effective height of the ionosphere layer (450 km)
h_{ref}	Reference elevation above which troposphere delay can be assumed unchanged
h_s	Satellite height
K	Constant with value 40.31 $m^3 s^-2$
K_r	Range chirp rate
k_1	Constant with value 0.776 KPa^-1
k_2	Constant with value 0.716 KPa^-1
k_3	Constant with value 3.75 $10^3 K^2 Pa^-1$
k_a	Azimuth FM-rate applied by the IPF processor
$k_{a,g}$	Annotated azimuth FM-rate at grid location t_g
$k_{a,true}$	True azimuth FM-rate mismatch
k_s	Doppler centroid rate at mid azimuth time
k_t	Doppler centroid rate
k_ψ	Azimuth steering rate of the antenna
m	Pixel location along range columns
m_{mid}	Number of range samples at mid-swath IW2
n	Pixel location along the azimuth lines
P	Dry air partial pressure
R_d	Specific gas constant for dry air
R_e	Earth radius
R_S	Vector describing sensor position in a xyz coordinate system
R_T	Vector describing target position in a xyz coordinate system
R_v	Specific gas constant for water vapor

r_0	Starting range (near range)
r	Slant range position (fast time)
$\hat{r}$	Estimated slant range position
r_{iono}	Ionospheric delay along LOS direction
r_{SET}	Solid Earth tide contribution along slant range
r^e_{SET}	Solid Earth tide displacement along east direction
r^n_{SET}	Solid Earth tide displacement along north direction
r^u_{SET}	Solid Earth tide displacement along up direction
r_{tropo}	Hydrostatic troposphere delay along LOS direction
T	Temperature (measured in Kelvin)
TEC	Total Electron Content
t_0	Azimuth start time
t	Zero Doppler azimuth time (slow time)
$\hat{t}$	Estimated azimuth time
t_{IPF}	Azimuth time from data annotation
t_{PRI}	Pulse repetition interval
t_{SET}	Solid Earth tide contribution along azimuth
t_{ref}	Reference azimuth time
V_S	Sensor velocity
$V_{S,mid}$	Sensor velocity computed at the mid azimuth time
x_S	Sensor position along x-direction
x_T	Target position along x-direction
y_S	Sensor position along y-direction
y_T	Target position along y direction
z_S	Sensor position along z-direction
β	Azimuth angle
β_{orb}	Azimuth angle of the satellite orbit
η_0	Vacuum refractive index
η_{IPP}	Refraction angle of the LOS vector
η_{iono}	Group refractive index of the ionosphere
θ	Incidence angle
θ_{IPP}	Incidence angle at the ionosphere piercing point
λ	Radar wavelength
ρ	Latitude coordinate
ρ_{IPP}	Latitude coordinate of the ionosphere piercing point
ρ_T	Target latitude coordinate
σ	Standard deviation
$\tau_{0,mid}$	First slant range time of the mid-swath IW2
τ	Slant range time
τ_g	Slant range time at the grid location g

τ_{mid}	Slant range time at mid-swath IW2
Φ	Longitude coordinate
Φ_{IPP}	Longitude coordinate of the ionosphere piercing point
Φ_T	Target longitude coordinate
ϕ	Chirp signal in the azimuth time domain
Δt_{BA}	Bistatic azimuth delay correction
Δt_{FMM}	Azimuth FM-rate mismatch correction
$\Delta \tau_{DRS}$	Doppler range shift correction
ZPD	Zenith Path Delay

11 Acknowledgements

This research was conducted at the Jet Propulsion Laboratory, California Institute of Technology, under contract with the National Aeronautics and Space Administration.
The original Copernicus Sentinel data used for this paper have been provided by the European Space Agency.

References

[1] R. N. Treuhaft and P. R. Siqueira, "Vertical structure of vegetated land surfaces from interferometric and polarimetric radar," *Radio Science*, vol. 35, no. 1, pp. 141–177, 2000.

[2] K. C. Kornelsen and P. Coulibaly, "Advances in soil moisture retrieval from synthetic aperture radar and hydrological applications," *Journal of Hydrology*, vol. 476, pp. 460–489, 2013.

[3] M. W. Becker, "Potential for satellite remote sensing of ground water," *Groundwater*, vol. 44, no. 2, pp. 306–318, 2006.

[4] W. Dierking, "Sea ice monitoring by synthetic aperture radar," *Oceanography*, vol. 26, no. 2, pp. 100–111, 2013.

[5] M. Tedesco, "Remote sensing and the cryosphere," *Remote Sensing of the Cryosphere*, pp. 1–16, 2015.

[6] P. A. Rosen, S. Hensley, I. R. Joughin, F. K. Li, S. N. Madsen, E. Rodriguez, and R. M. Goldstein, "Synthetic aperture radar interferometry," *Proceedings of the IEEE*, vol. 88, no. 3, pp. 333–382, 2000.

[7] R. Bürgmann, P. A. Rosen, and E. J. Fielding, "Synthetic aperture radar interferometry to measure Earths surface topography and its deformation," *Annual review of earth and planetary sciences*, vol. 28, no. 1, pp. 169–209, 2000.

[8] V. Pinel, M. P. Poland, and A. Hooper, "Volcanology: Lessons learned from synthetic aperture radar imagery," *Journal of Volcanology and Geothermal Research*, vol. 289, pp. 81–113, 2014.

[9] C. Colesanti and J. Wasowski, "Investigating landslides with space-borne Synthetic Aperture Radar (SAR) interferometry," *Engineering geology*, vol. 88, no. 3-4, pp. 173–199, 2006.

[10] J. Hoffmann, H. A. Zebker, D. L. Galloway, and F. Amelung, "Seasonal subsidence and rebound in Las Vegas Valley, Nevada, observed by synthetic aperture radar interferometry," *Water Resources Research*, vol. 37, no. 6, pp. 1551–1566, 2001.

[11] J. Mouginot, E. Rignot, and B. Scheuchl, "Continent-wide, interferometric SAR phase, mapping of Antarctic ice velocity," *Geophysical Research Letters*, vol. 46, no. 16, pp. 9710–9718, 2019.

[12] J. C. Curlander and R. N. McDonough, *Synthetic aperture radar*. Wiley, New York, 1991, vol. 11.

[13] D. Just and R. Bamler, "Phase statistics of interferograms with applications to synthetic aperture radar," *Applied optics*, vol. 33, no. 20, pp. 4361–4368, 1994.

[14] F. De Zan, "Accuracy of incoherent speckle tracking for circular Gaussian signals," *IEEE Geoscience and Remote Sensing Letters*, vol. 11, no. 1, pp. 264–267, 2013.

[15] E. Sansosti, P. Berardino, M. Manunta, F. Serafino, and G. Fornaro, "Geometrical SAR image registration," *IEEE Transactions on Geoscience and Remote Sensing*, vol. 44, no. 10, pp. 2861–2870, 2006.

[16] H. Fattahi, M. Simons, and P. Agram, "InSAR time-series estimation of the ionospheric phase delay: An extension of the split range-spectrum technique," *IEEE Transactions on Geoscience and Remote Sensing*, vol. 55, no. 10, pp. 5984–5996, 2017.

[17] R. Scheiber and A. Moreira, "Coregistration of interferometric SAR images using spectral diversity," *IEEE Transactions on Geoscience and Remote Sensing*, vol. 38, no. 5, pp. 2179–2191, 2000.

[18] Z. Yunjun, H. Fattahi, X. Pi, P. Rosen, M. Simons, P. Agram, and Y. Aoki, "Range geolocation accuracy of C-/L-Band SAR and its implications for operational stack coregistration," *IEEE Transactions on Geoscience and Remote Sensing*, vol. 60, pp. 1–19, 2022.

[19] C. Gisinger, A. Schubert, H. Breit, M. Garthwaite, U. Balss, M. Willberg, D. Small, M. Eineder, and N. Miranda, "In-depth verification of Sentinel-1 and TerraSAR-X geolocation accuracy using the Australian corner reflector array," *IEEE Transactions on Geoscience and Remote Sensing*, vol. 59, no. 2, pp. 1154–1181, 2020.

[20] Y. Zheng and H. A. Zebker, "Phase correction of single-look complex radar images for user-friendly efficient interferogram formation," *IEEE Journal of Selected Topics in Applied Earth Observations and Remote Sensing*, vol. 10, no. 6, pp. 2694–2701, 2017.

[21] H. A. Zebker, "User-friendly InSAR data products: Fast and simple time-series processing," *IEEE Geoscience and Remote Sensing Letters*, vol. 14, no. 11, pp. 2122–2126, 2017.

[22] F. De Zan and A. M. Guarnieri, "TOPSAR: Terrain observation by progressive scans," *IEEE Transactions on Geoscience and Remote Sensing*, vol. 44, no. 9, pp. 2352–2360, 2006.

[23] P. Vincent, M. Bourbigot, H. Johnsen, and R. Piantanida, "Sentinel-1 product specification," *moz-extension://f411f992-5fa2-42c1-9208-0af48b9cac28/enhancedreader. html*, 2019.

[24] C. Gisinger, L. Libert, P. Marinkovic, L. Krieger, Y. Larsen, A. Valentino, H. Breit, U. Balss, S. Suchandt, T. Nagler *et al.*, "The extended timing annotation dataset for Sentinel-1: Product description and first evaluation results," *IEEE Transactions on Geoscience and Remote Sensing*, vol. 60, pp. 1–22, 2022.

[25] R. Piantanida, "Sentinel-1 level 1 detailed algorithm definition," 2022. [Online]. Available: https://sentinels.copernicus.eu/documents/247904/1877131/S1-TN-MDA-52-7445_Sentinel-1+Level+1+Detailed+Algorithm+Definition_v2-5.pdf/41ddb893-ba7f-2078-6c87-d1374e3093e1?t=1669830527097

[26] M. Rodriguez-Cassola, P. Prats-Iraola, F. De Zan, R. Scheiber, A. Reigber, D. Geudtner, and A. Moreira, "Doppler-related distortions in TOPS SAR images," *IEEE Transactions on Geoscience and Remote Sensing*, vol. 53, no. 1, pp. 25–35, 2014.

[27] N. Miranda, B. Rosich, and C. Putignano, "The sentinel-1 data processor and operational products," in *2012 IEEE International Geoscience and Remote Sensing Symposium*, 2012, pp. 1730–1733.

[28] P. Teunissen and O. Montenbruck, "Handbook of Global Navigation Satelite Systems," *Springer International Publishing AG. DOI*, vol. 10, pp. 978–3, 2017.

[29] G. Petit and B. Luzum, "IERS technical note no. 36, IERS conventions (2010)," *International Earth Rotation and Reference Systems Service: Frankfurt, Germany*, 2010.

[30] P. A. Wright, S. Quegan, N. S. Wheadon, and C. D. Hall, "Faraday rotation effects on L-band spaceborne SAR data," *IEEE Transactions on Geoscience and Remote Sensing*, vol. 41, no. 12, pp. 2735–2744, 2003.

[31] J. S. Shim, *Analysis of total electron content (TEC) variations in the low-and middle-latitude ionosphere*. Utah State University, 2009.

[32] J. Böhm and H. Schuh, *Atmospheric effects in space geodesy*. Springer, 2013, vol. 5.

[33] M. Hernández-Pajares, J. Juan, J. Sanz, R. Orus, A. Garcia-Rigo, J. Feltens, A. Komjathy, S. Schaer, and A. Krankowski, "The IGS VTEC maps: a reliable source of ionospheric information since 1998," *Journal of Geodesy*, vol. 83, pp. 263–275, 2009.

[34] H. Berrada Baby, P. Gole, and J. Lavergnat, "A model for the tropospheric excess path length of radio waves from surface meteorological measurements," *Radio science*, vol. 23, no. 6, pp. 1023–1038, 1988.

[35] H. A. Zebker, P. A. Rosen, and S. Hensley, "Atmospheric effects in interferometric synthetic aperture radar surface deformation and topographic maps," *Journal of geophysical research: solid earth*, vol. 102, no. B4, pp. 7547–7563, 1997.

[36] R. F. Hanssen, *Radar interferometry: data interpretation and error analysis*. Springer Science & Business Media, 2001, vol. 2.

[37] M. Jehle, D. Perler, D. Small, A. Schubert, and E. Meier, "Estimation of atmospheric path delays in TerraSAR-X data using models vs. measurements," *Sensors*, vol. 8, no. 12, pp. 8479–8491, 2008.

[38] H. Hersbach, B. Bell, P. Berrisford, S. Hirahara, A. Horányi, J. Muñoz-Sabater, J. Nicolas, C. Peubey, R. Radu, D. Schepers *et al.*, "The ERA5 global reanalysis," *Quarterly Journal of the Royal Meteorological Society*, vol. 146, no. 730, pp. 1999–2049, 2020.

[39] H. Breit, T. Fritz, U. Balss, M. Lachaise, A. Niedermeier, and M. Vonavka, "TerraSAR-X SAR processing and products," *IEEE Transactions on Geoscience and Remote Sensing*, vol. 48, no. 2, pp. 727–740, 2009.

[40] M. Eineder, C. Minet, P. Steigenberger, X. Cong, and T. Fritz, "Imaging geodesy: Toward centimeter-level ranging accuracy with TerraSAR-X," *IEEE Transactions on Geoscience and Remote Sensing*, vol. 49, no. 2, pp. 661–671, 2010.

[41] N. Miranda, "Definition of the TOPS SLC deramping function for products generated by the S-1 IPF," *ESA Technical Note*, 2014.

[42] S. D. Kropatsch, W. G., "The generation of SAR layover and shadow maps from digital elevation models," *IEEE Transactions on Geoscience and Remote Sensing*, vol. 28, no. 1, pp. 98–107, 1990.

[43] M. Schwerdt, K. Schmidt, N. T. Ramon, G. C. Alfonzo, B. J. Döring, M. Zink, and P. Prats-Iraola, "Independent verification of the Sentinel-1A system calibration," *IEEE Journal of Selected Topics in Applied Earth Observations and Remote Sensing*, vol. 9, no. 3, pp. 994–1007, 2015.

[44] A. Schubert, D. Small, N. Miranda, D. Geudtner, and E. Meier, "Sentinel-1A product geolocation accuracy: Commissioning phase results," *Remote sensing*, vol. 7, no. 7, pp. 9431–9449, 2015.

[45] S. J. Orfanidis, "Electromagnetic waves and antennas," 2002.

[46] C. Liang, P. Agram, M. Simons, and E. J. Fielding, "Ionospheric correction of InSAR time series analysis of C-band Sentinel-1 TOPS data," *IEEE Transactions on Geoscience and Remote Sensing*, vol. 57, no. 9, pp. 6755–6773, 2019.

[47] G. Gomba, A. Parizzi, F. De Zan, M. Eineder, and R. Bamler, "Toward operational compensation of ionospheric effects in SAR interferograms: The split-spectrum method," *IEEE Transactions on Geoscience and Remote Sensing*, vol. 54, no. 3, pp. 1446–1461, 2015.

[48] P. A. Rosen, E. M. Gurrola, P. Agram, J. Cohen, M. Lavalle, B. V. Riel, H. Fattahi, M. A. Aivazis, M. Simons, and S. M. Buckley, "The InSAR scientific computing environment 3.0: a flexible framework for NISAR operational and user-led science processing," in *IGARSS 2018-2018 IEEE International Geoscience and Remote Sensing Symposium*. IEEE, 2018, pp. 4897–4900.

[49] D. Milbert, "Solid: Solid earth tide," *SOFTS/solid. htm*, 2018.